An Integral Battery Charger with Power Factor Correction for Electric Scooter

An Integral Battery Charger with Power Factor Correction for Electric Scooter

G. Pellegrino, E. Armando and P. Guglielmi

Politecnico di Torino

C.so Duca degli Abruzzi 24, 10129, Torino, Italy

Emails: (gianmario.pellegrino, eric.armando, paolo.guglielmi)@polito.it

Keywords:

Battery chargers, Road vehicle electric propulsion, AC-DC power conversion, AC motor drives.

ABSTRACT

The paper presents an integral battery charger for an electric scooter with high voltage batteries and Interior-Permanent-Magnet (IPM) motor traction drive. The battery charger is derived from the power hardware of the scooter, with the AC motor drive that operates as three-phase boost rectifier with Power Factor Correction (PFC) capability. The control of the charger is also integrated into the scooter control firmware that is implemented on a fixed-point DSP controller. Current-controlled or voltage-controlled charge modes are actuated according to the requirements of the Battery Management System (BMS), that is embedded into the battery pack. Respect to previous integrated chargers, the AC current is absorbed at unitary power factor with no harmonic distortion. Moreover, no additional filtering is needed since the PWM ripple is minimized by means of phase interleaving. The feasibility of the integral charger with different AC motors (Induction Motor, Surface-Mounted PM motor) is also discussed, by means of a general model purposely developed for 3-phase AC machines. The effectiveness of the proposed battery charger is experimentally demonstrated on a prototype electric scooter, equipped with two Li-Ion battery packs rated 260 V, 20 Ah.

I. INTRODUCTION

The traction battery is the most critical component of an electric vehicle: the cost, the weight as well as the driving range and the reliability of the vehicle are strongly influenced by the characteristics of the battery. Moreover, the battery must be properly managed, and in particular properly recharged, for obtaining the exploitation of its full capacity and for the respect of its nominal lifetime.

On-board battery chargers must have reduced weight and the volume, since they are carried by the vehicle. They are usually capable of charging the batteries in a couple of hours by means of a single-phase AC source, like the household utility outlet. In recharge, the battery current and voltage must be regulated according to the

specifications of the manufacturer and according to the estimated state of charge. Last, the absorbed AC current must respect the international standards of unitary power factor and low harmonics distortion [1], [2].

The integral battery charger is obtained from the power conversion hardware of an electric scooter with very few additional components. Integrated chargers have been proposed by different authors [3]–[6]. In particular, the idea of accessing the motor center tap for using the motor as a coupling inductor was first introduced in [4] and [5], for electric cars with multiple AC motor drives. A simpler conversion topology was proposed for an electric scooter in [6], where the center tap of the motor is connected to a rectifier via a mechanical switch, and the traction inverter is operated as a dc-dc boost battery charger. A similar topology is applied here to a scooter with Interior Permanent Magnet (IPM) motor traction drive with a series of significant improvements:

- the Power-Factor-Correction capability;
- the interleaving of the three inverter phases, that minimizes the PWM ripple and improves the control dynamics of the PFC rectifier;
- the modeling of the IPM motor as a feasible coupling inductor;
- the investigation of what should happen with different traction motors (Induction Motor, Surface-Mounted PM motor), by means of a general modeling approach.

The AC motor drive is operated here as a PFC boost rectifier where the motor works as a 3-phase coupled inductor. The adoption of phase interleaving strongly reduces the current ripple and improves the control dynamics [7], [8], in particular with mutually-coupled inductors as it is the case here [9], [10].

The scooter prototype is a big urban scooter (2 persons, 90 km/h max), equipped with two Lithium-Ion battery packs (260V, 10Ah each) with individual DC/DC stages. Detailed ratings are reported in the Appendix.

The paper is organized as follows. In section II the integrated battery charger is presented and described in detail with particular attention to the modeling of the 3-phase boost rectifier. In section III the integration of the PFC rectifier control is described. In section IV the experimental results are presented and commented.

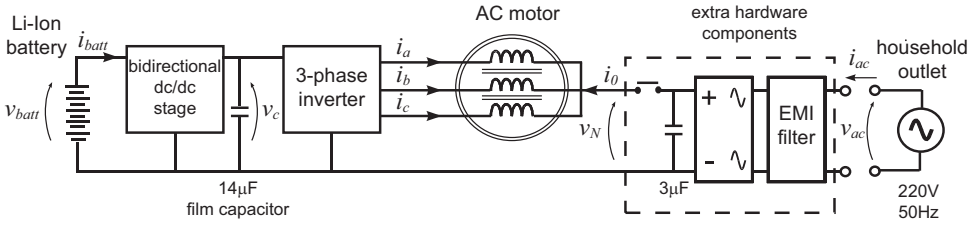

Fig. 1. Integrated battery charger: the traction drive is transformed into a 3-phase PFC boost battery charger.

II. Integral battery charger

The basic electric scooter powertrain is represented in Fig. 1. It consists of the AC motor drive plus a bidirectional DC/DC stage: in charge operation, the AC drive becomes the PFC rectifier, while the DC/DC stage still actively controls the v_c voltage. In the prototype, the battery packs are two with two DC/DC converters, but this makes no

difference in the following analysis. The *extra hardware components* evidenced in the figure are representative of the hardware that is needed for adapting the traction drive to the charge purpose: they are a single-phase rectifier bridge with a mechanical switch to access the center tap of the motor, a 3 μF capacitor and an EMI filter. The measure of the rectified voltage (v_N) is also needed. All the other measures by the power charger are already available for the control of the motor drive.

The single-phase AC source introduces a large input power component at 100 Hz that can not be accumulated by the small dc-link capacitor (14 μF) represented in Fig. 1: thus a corresponding 100 Hz component is produced on the battery current, while the dc-link voltage is regulated at a constant value by the DC/DC stage. There is no need of a specific control algorithm for the DC/DC since its mission is to regulate the dc-link voltage also during traction operation.

A. 3-phase boost converter

The circuit reported in Fig. 2 describes the boost converter obtained from the IPM motor drive, where abc are the motor terminals and the neutral point N is the input terminal. The phase currents maintain the motor notation, as do the measures available for the control. As said, V_c is constant. The input current will be regulated by means of the inverter common-mode voltage, while the differential-mode current components will be regulated to zero for current balancing according to the approach proposed in [11], [12]. The high side IGBTs are not enabled, since no discontinuous current operation occurs in practical implementation. The phase switching frequency is 20 kHz.

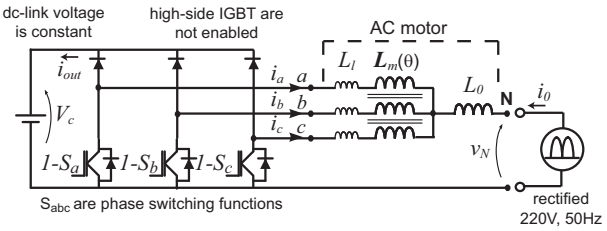

Fig. 2. Three-phase boost converter obtained by the IPM motor traction drive.

B. 4-wire model of the IPM motor drive.

The non-conventional 3-phase boost converter represented in Fig. 2 is modeled by the state equation (1).

$$\frac{d\boldsymbol{\lambda}_{abc}}{dt} + R \cdot \mathbf{i}_{abc} = \mathbf{S}_{abc} \cdot V_c - v_N \tag{1}$$

Where $\boldsymbol{\lambda}_{abc}, \mathbf{i}_{abc}$ are column vectors representative of the motor phase fluxes and currents respectively, R is the motor phase resistance and $\mathbf{S}_{abc}$ is the vector of the inverter switching functions. The current to flux model of the motor (2) consists of the three inductance terms also evidenced in Fig. 2: leakage inductance L_l, magnetizing inductances $\mathbf{L}_m(\theta)$ and zero-sequence inductance $\mathbf{L}_0$. The permanent-magnet flux is not represented in (2) because

it gives no flux-derivative (i.e. voltage) contribution when the motor is steady. The inductance matrix is expressed in detail in (3).

$$\boldsymbol{\lambda}_{abc} = [L_l + \mathbf{L}_m(\theta) + \mathbf{L}_0] \cdot \mathbf{i}_{abc} \tag{2}$$

$$L_l + \mathbf{L}_m(\theta) + \mathbf{L}_0 = \begin{bmatrix} L_l + L_0 + L_{ma} & L_0 + L_{mab} & L_0 + L_{mca} \\ L_0 + L_{mab} & L_l + L_0 + L_{mb} & L_0 + L_{mbc} \\ L_0 + L_{mca} & L_0 + L_{mbc} & L_l + L_0 + L_{mc} \end{bmatrix} \tag{3}$$

In Fig. 3-a the dq reference frame is defined respect to the phase motor axes abc. Since the motor is anisotropic, the phase inductances depend on the rotor electrical position θ as plotted in Fig. 3-b for the motor under test. The relationship between the abc model and the bi-phase model in the dq synchronous frame is reported in (4).

$$\mathbf{L}_m(\theta) = \frac{L_{md} + L_{mq}}{2} \cdot \begin{bmatrix} 1 & -\frac{1}{2} & -\frac{1}{2} \\ -\frac{1}{2} & 1 & -\frac{1}{2} \\ -\frac{1}{2} & -\frac{1}{2} & 1 \end{bmatrix} - \frac{L_{md} - L_{mq}}{2} \cdot cos(2\theta + \begin{bmatrix} 0 & -\frac{2\pi}{3} & +\frac{2\pi}{3} \\ -\frac{2\pi}{3} & +\frac{2\pi}{3} & 0 \\ +\frac{2\pi}{3} & 0 & -\frac{2\pi}{3} \end{bmatrix}) \tag{4}$$

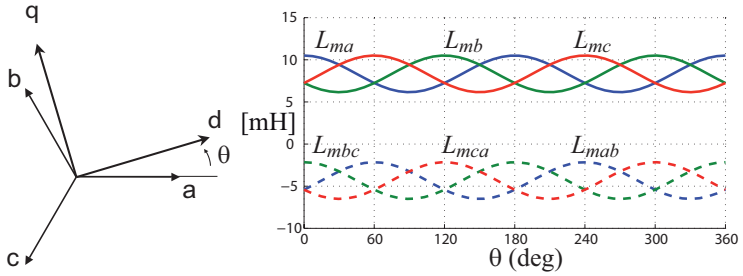

(a) (b)

Fig. 3. a) Reference axes definition. b) Inductances of the IPM motor under test versus rotor electrical position θ. L_{md} = 6mH, L_{mq} = 10.5mH.

C. Common-mode and differential-mode approach.

It is convenient to redefine the motor phase currents as in (5), where the input current i_0 (common-mode component) has been separated from the residual or differential-mode current components, that are indicated with the superscript $'$. The magnetic model (2) is rewritten accordingly (6).

$$\mathbf{i}_{abc} = \mathbf{i}'_{abc} - i_0/3 \tag{5}$$

$$\boldsymbol{\lambda}_{abc} = (L_l + \mathbf{L}_m(\theta)) \cdot \mathbf{i}'_{abc} - (L_l/3 + L_0) \cdot i_0 \tag{6}$$

The current components put in evidence in (5) and (6) will be respectively controlled for obtaining a balanced current sharing ($\mathbf{i}'_{abc} = 0$) and the PFC power conversion ($i_0 = I_0 \cdot |sin(\omega t)|$, where ω is the angular frequency of the AC mains). The boost converter dynamics is described in the new current components by the two state equations (7a)-(7b) obtained by substituting (6) in (1).

$$(L_l/3 + L_0) \cdot \frac{di_0}{dt} + R/3 \cdot i_0 = v_N - V_c \cdot S_0 \tag{7a}$$

$$(L_l + \mathbf{L}_m(\theta)) \cdot \frac{d\mathbf{i}'_{abc}}{dt} + R \cdot \mathbf{i}'_{abc} = \mathbf{S}'_{abc} \cdot V_c \tag{7b}$$

Where S_0 and $\mathbf{S}'_{abc}$ are the common and differential-mode switching functions respectively. The two equations are summarized by the two schematics in Fig. 4.

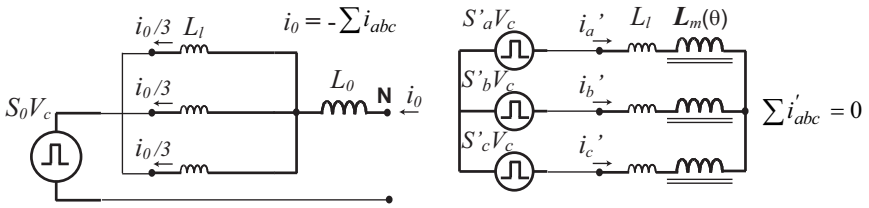

(a) common-mode (b) differential-mode

Fig. 4. Common-mode (boost) and differential-mode (3-wire AC motor) models of the IPM motor drive.

In particular, as reported in (8), S_0 can assume four discrete values that stand for the multi-level capability of the boost converter.

$$S_0 = \frac{1}{3} \cdot \sum_{j=a,b,c} S_j = \frac{(0,1,2,3)}{3} \tag{8}$$

It is worthy to note that the rotor position does not appear in (7a) since the $\mathbf{L}_m(\theta)$ matrix has no zero-sequence component: thus *it is demonstrated that the anisotropy of the motor gives has no side effect on the boost converter dynamics, as the motor was a symmetrical coupled inductor*. The average value of S_0, or *common-mode duty-cycle* (9), is the input to output voltage transfer ratio of the converter.

$$D_0 = \int_0^{T_s} S_0 \cdot dt \cong \frac{V_N}{V_c} \tag{9}$$

Where T_s is the PWM switching period, the resistive term has been neglected and V_N stands for the average of v_N in T_s.

D. Phase currents equalization.

The differential-mode equation (7b) represents the AC drive with no zero-sequence, or the 3-wire motor when the center tap is insulated as in Fig. 4b. For the sake of current control, this model is usually described in d, q coordinates (10), in the already introduced synchronous frame.

$$\begin{bmatrix} L_d & 0 \\ 0 & L_q \end{bmatrix} \cdot \frac{d\mathbf{i}_{dq}}{dt} + R \cdot \mathbf{i}_{dq} = \mathbf{i}_{dq} \tag{10}$$

Where $L_d = L_l + L_{md}$, $L_q = L_l + L_{mq}$. During battery charge, the d, q current components are controlled to zero by means of the d, q vector control of the AC drive and this keeps the phase currents balanced (11).

$$I_d, I_q = 0 \Leftrightarrow I'_a, I'_b, I'_c = 0 \Rightarrow I_a = I_b = I_c \tag{11}$$

The capital letters in (11) indicate that the average currents are zero, but still a ripple component remains, and its contribution varies from phase to phase due to motor anisotropy as will be seen in subsection III.F.

E. Phase interleaving.

The phase switching commands are regularly spaced as in Fig. 5, where S_0 and the phase component S'_a are also plotted. The following considerations summarize the effects of phase interleaving in the considered converter:

- the modulation frequency of the input and output currents is three times the phase switching frequency (20 $\times$ 3 = 60 kHz in this case);
- consequently, the input and output current ripples are strongly reduced;
- the input current ripple is zero for singular voltage ratios ($v_N = 1/3, 2/3 \cdot V_c$);
- the differential-mode voltages are alternative signals at the fundamental PWM frequency (S'_a in Fig. 5);
- as a consequence, they produce a phase current ripple at 20 kHz;
- phase mutual coupling improves the conversion efficiency and the control dynamics [13].

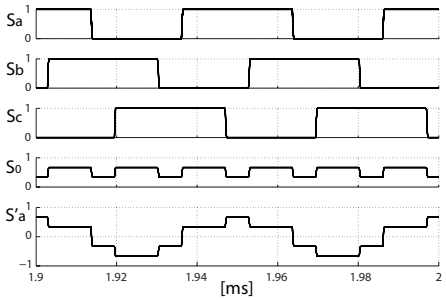

Fig. 5. Interleaved switching commands $\mathbf{S}_{abc}$ for $D_0 = 0.56$: S_0 is the common-mode switching function and S'_a is the differential-mode switching function of phase a.

As an example, the current waveforms of the interleaved converter are reported in Fig. 6 for 5 A input current, in steady-state, in three different D_0 situations that produce the same input ripple.

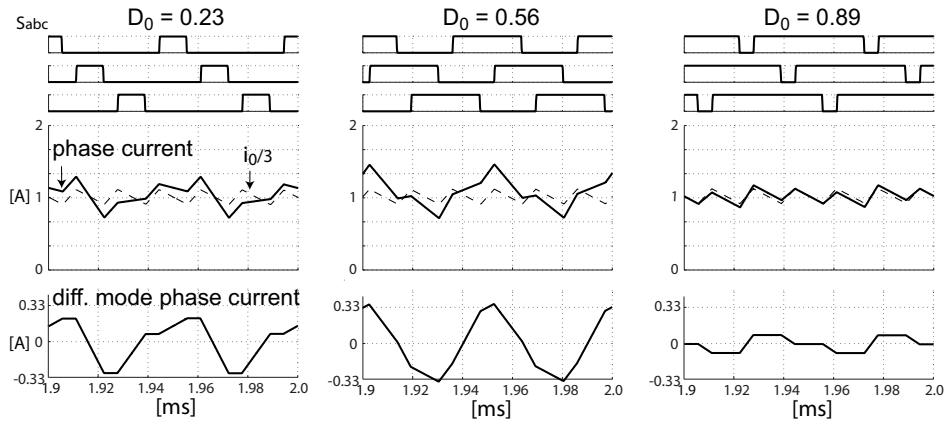

Fig. 6. Current waveforms with phase interleaving. Three steady state situations are represented, with the same input current and duty-cycles chosen for having exactly the same i_0 ripple in three cases. The differential-mode ripple component is evidenced for one of the phases.

F. Current ripple and effect of the rotor saliency.

The input current ripple varies as a function of the duty-cycle D_0 as reported in Fig. 7, that refers to steady-state, peak to peak ripple. The non-interleaved situation is also represented for the sake of comparison. The plots has been obtained by integrating (7a) over the switching period like suggested in [12]. As already demonstrated in subsection II-C, the rotor anisotropy has no effect on i_0. The effect of rotor position due to the anisotropy is visible in the differential-mode currents only, because they depend on the $\mathbf{L}_m(\theta)$ inductances according to (7b). Two extreme situations are found: when one phase is aligned to the d axis its inductance is minimal, i.e. the current ripple is maximum, while when the same phase is aligned to the q axis the minimum ripple occurs. Also the differential-mode ripple depends on D_0, as suggested by Fig. 6. The amplitude of the differential-mode phase ripple is represented in steady-state in Fig. 8 for the prototype under test: the worst case (phase aligned to d) and best case (phase aligned to q) plots are reported. They have been obtained by integrating equation (7b) after substituting (4). All the drive parameters needed for the calculations can be found in the Appendix.

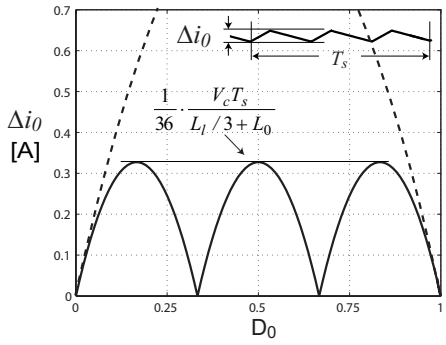

Fig. 7. Peak to peak amplitude of the input current ripple. Continuous line: with phase interleaving. Dashed line: without phase interleaving.

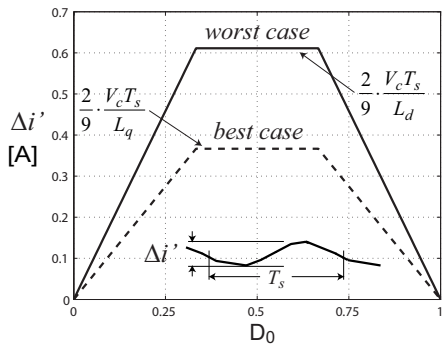

Fig. 8. Peak to peak amplitude of the residual phase ripple (differential-mode). Continuous line: worst case situation (phase aligned to d), dashed line: best case situation (phase aligned to q).

G. Feasibility with different motor types.

Other types of AC motors can be considered for electric vehicles, namely Surface Mounted PM (SMPM) motors and IM motors [14]. Dealing with SMPM motors, the thick air-gap (air-gap plus magnet lenght) reduces both the zero-sequence and the phase inductances, thus a higher current ripple is expected both on the input and the phase currents according to the formulas in Fig. 7 and Fig. 8. Due to low inductances, the converter dynamics is fast but the high ripple results in discontinuous current operation around zero current that complicates the control of the PFC rectifier. A particular case is represented by SMPM machines with concentrated windings, that show higher inductance values, due to a relevant leakage term [15]. The high inductance reduces the ripple, but still the PFC control dynamics tends to be slow: the differential-mode inductance ($L_l + \mathbf{L}_m$) is high due to L_l and not to $\mathbf{L}_m$, but also the common-mode term ($L_l/3 + L_0$) is high.

Dealing with Induction Motor drives (IM), the rotor equation should be also considered in addition to (1) and its following developments (7a), (7b) and (10). Since the rotor windings have no zero-sequence current, it can be demonstrated that the common-mode state equation is exactly the same as (7a), where the stator leakage inductance and the stator resistance must be considered as for the IPM motor. The rotor behavior appears in the differential-mode model only. The differential-mode phase voltages are at PWM frequency (20 kHz, see Fig. 5), and the short-circuited rotor cage reacts to the arising of differential-mode currents with corresponding currents like in a short-circuited transformer. For a comprehensive description of such operating conditions, the skin effect in the rotor bars and the high-frequency core losses should be also included into the model, but it can be demonstrated that the differential-mode inductance of the motor as it is seen from the stator terminals approximately equals the rated short-circuit inductance (stator leakage plus rotor leakage), measured with the blocked-rotor test at industrial frequency. The dq stator model (10) is still valid for our purposes, where the low short-circuit inductance substitutes the L_d and L_q terms. The experimental identification of a 4 kW, 1450 rpm, 50 Hz industrial IM, with the procedure described in subsection IV.A, has confirmed the assumptions over the IM model. A low differential-mode inductance leads to a high phase current ripple, according to the formulas in Fig. 8. As for the SMPM motor, discontinuous current operation is expected around zero current due to the high ripple. It is suggested to command all the inverter

switches in this case (high side included) to avoid it and its side effects on the PFC control. Nevertheless, a lower efficiency and a bigger EMI filter are expected.

III. Integrated control of the PFC battery charger.

The control scheme of the PFC boost rectifier is reported in Fig. 9. The unitary power factor at the AC side is obtained by the synchronization of the input current i_0 with the rectified AC voltage ($v_N = |v_{ac}|$). The measured quantities are the motor phase currents, the dc-link voltage and the input voltage v_N. Apart for the PWM ripple that is minimized by phase interleaving and filtered by the 3μF input capacitor and the EMI filter, the Total Harmonic Distortion (THD) factor of the AC current relies on the performance of the current controller. The current amplitude set point I_0^* is provided by the Battery Management System (BMS) with a maximum of 8.5A (pk) that corresponds to nearly $1350W$ maximum power absorbed from the household outlet. The BMS is embedded in the battery stack and it is capable of monitoring the voltage of all the elements in series in real time [16]. As introduced in section III, the d, q current controller of the IPM motor drive guarantees the current sharing equalization. The PWM units have individual interleaved counters that are used for synchronization of the switching commands and of the motor currents sampling. In the presented prototype the control of all the scooter converters (double DC/DC plus 3-ph inverter) is managed by an industrial DSP (Freescale 56F801), while all the PWM and analog to digital functions are implemented on a FPGA. Nevertheless, many up-to-date DSP controllers can manage individual timebases for PWM and A/D sampling. The dc-link is controlled at 330V that is 20V higher than the AC mains peak so that the boost regulation range is fully exploited (D_0 spans from zero to 0.94, more or less).

A. Input current control

The input current control scheme is reported in the upper part of Fig. 9. The current reference amplitude is given by the BMS. The current regulator is of the Proportional-Integral type and needs the feed-forward term v_{ff} for obtaining a good tracking of the reference current, in particular around zero where the slope of i_0^* is discontinuous [17], [18]. As clearly explained in [17], the feed-forward should include a load-dependent term due to the series inductance drop at 50Hz ($L_0+L_l/3$ plus the EMI filter), thus v_{ff} should be delayed respect to v_N proportionally with the load current, with little amplitude modification. Once the feed-forward is correctly calculated, the PI regulator should only compensate for minor errors and non-idealities. In practical implementation it must be considered that:

- the inductive drop at 50Hz is very small (4 Vpk with 8.5 Apk line current) thus the time delay of the feed-forward would be 40 μs at maximum load;
- the PWM discretization introduces a time delay (50 μs) that practically coincides with the one required at full load.

For these reasons in the prototype the v_N measure is directly added in feed-forward, with no load-dependent delay ($v_{ff} = v_N$).

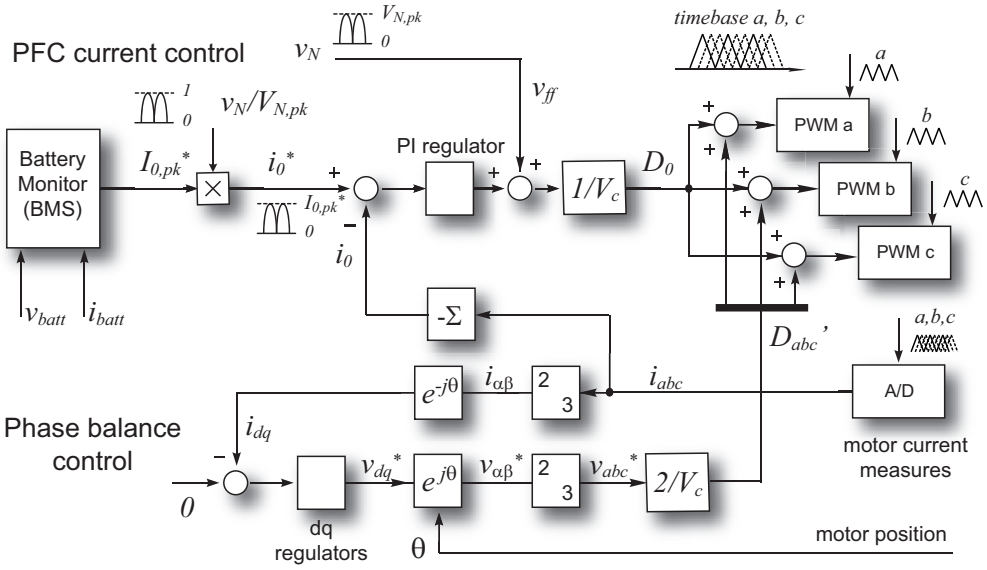

Fig. 9. Current control of the PFC boost battery charger with interleaved phases.

B. $d-q$ control and current equalization

The d, q vector control of the IPM motor equalizes the phase currents with no modification, apart for the already discussed PWM synchronization. The 3-phase to 2-phase transformation evidenced in the lower part of Fig. 9 eliminates the zero current sequence thus the differential-mode duty cycles that are added to the D_0 reference differ from zero only for reacting to eventual current unbalance.

IV. Experimental results

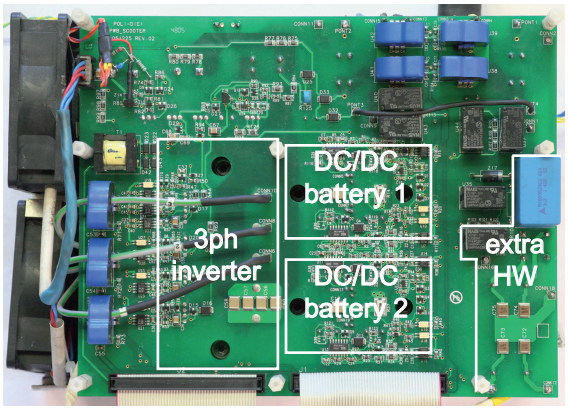

Fig. 10. Power board of the electric scooter: the extra hardware components of the battery charger are put in evidence.

The power board of the scooter is reported in Fig. 10. The board size is 175mm $\times$ 220mm and includes all the converters of the scooter: the 3-phase inverter and two H-Bridge DC/DC stages, one per battery pack. The extra hardware components for battery charge operation are evidenced on the right side of the figure.

A. Identification of the IPM motor at PWM frequency

The 4-wire model of the IPM motor has been identified by means of square wave excitation around the PWM frequency. The test conditions are described in Fig. 11. The zero-sequence inductance is evaluated at 20 kHz as described in Fig. 12. The current discontinuity at the voltage reversal stands for iron loss effects. The inductance evaluated at 20 kHz is 1.4 mH but the apparent inductance at 60 kHz is lower due to iron loss.

The results of the differential-mode test are reported for two different rotor positions in Fig. 13. The test frequency is 1kHz for the complete visualization of the iron loss transient. The asymptotic $q-$axis inductance corresponds to the steady-state value reported in the Appendix (44 mH) while the apparent inductance at 20 kHz is significantly lower (10 mH). The L_d measure is practically not affected by iron loss effect, and coincides with the steady-state value (6 mH). As a result, the effect of the iron losses reduces the apparent motor anisotropy at high frequency despite the high magnetic saliency of the rotor. In Fig. 13 the phase to neutral voltage is also reported: its asymptotic value does not depend on the motor position, as demonstrated by the term S_0V_c in equation (7a), but the transient evolutions of Fig. 13(a) and (b) are different due to the iron losses that are not considered in the model.

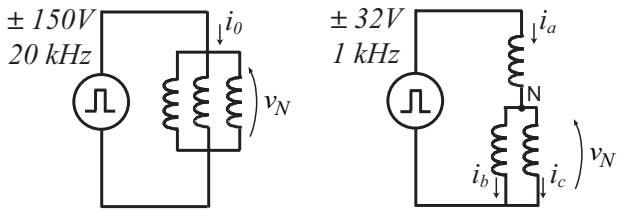

(a) common-mode test (b) differential-mode test

Fig. 11. Square-wave tests for the evaluation of common-mode and differential-mode inductances.

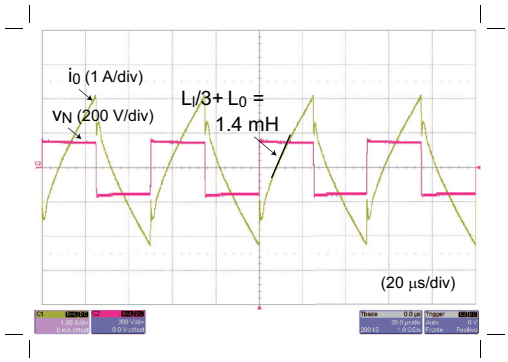

Fig. 12. Square wave test (20 kHz) for the evaluation of the zero-sequence inductance.

B. Performance of the PFC charger.

The experimental setup for testing the PFC performance is reported in Fig. 14. The AC plug and the two battery packs are evidenced. A multi-channel digital watt-meter measures the AC input power and the power of the two batteries synchronously to evaluate the overall efficiency.

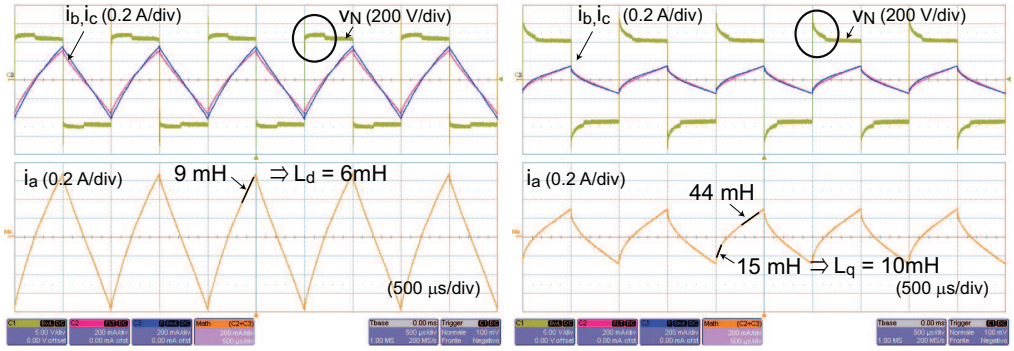

(a) d-axis (b) q-axis

Fig. 13. Square wave test (1 kHz) for the evaluation of the differential-mode inductances L_d, L_q at 20 kHz.

In Fig. 15 and Fig. 16 a full power recharge is reported in two different rotor positions. The AC current waveform is directly comparable to the AC input voltage in the two figures. The current perturbation around the zero-crossing is due to some imprecision in the feedforward term. The ripple of i_0 evidences the two singular situations around $D_0 = 1/3$ and $D_0 = 2/3$ described in Fig. 7. The PWM ripple on the AC current is negligible. The phase current is one third of the total current in the two figures due to the active current equalization. As expected, the phase current ripple is smaller when the phase is aligned with q (Fig. 15) and larger when it is aligned with d (Fig. 16) but the two situations are not so different due to the low apparent anisotropy of the motor at 20 kHz.

The current of one battery pack is reported in Fig. 17 with its evident 100 Hz component whose consequences on the battery life and performance are still under investigation and also differ from one battery technology to another [19], [20]. The prototype batteries did not evidence any significant side effect so far. The modulation ripple is produced by the DC/DC stage that regulates the dc-link voltage. The ripple has a constant amplitude since the battery to dc-link voltage ratio is constant and the DC/DC practically works at a constant duty-cycle.

Finally, the measured efficiency is reported in Fig. 18 as a function of the AC input power. The sum of the two battery powers has been considered as the output power. Since most of the losses are independent of the converted

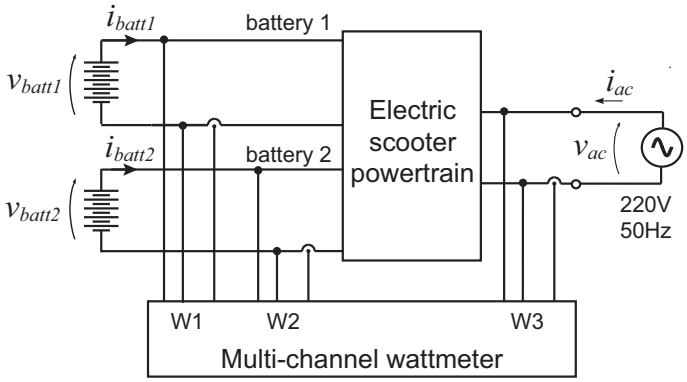

Fig. 14. Experimental setup.

power, the efficiency of the battery charger is higher at high loads.

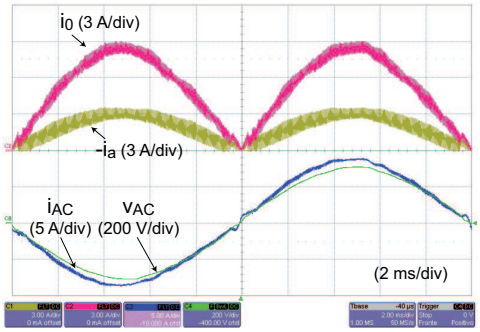

Fig. 15. PFC performance: the d axis is aligned with the phase a of the motor, the current ripple in a is maximum.

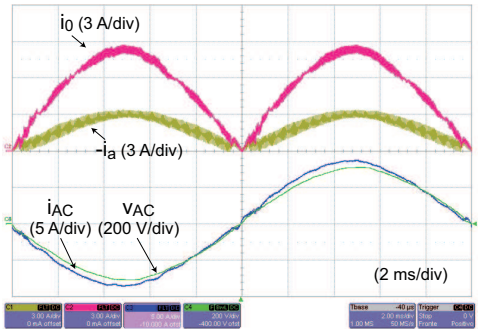

Fig. 16. PFC performance: the q axis is aligned with the phase a of the motor, the current ripple in a is minimum.

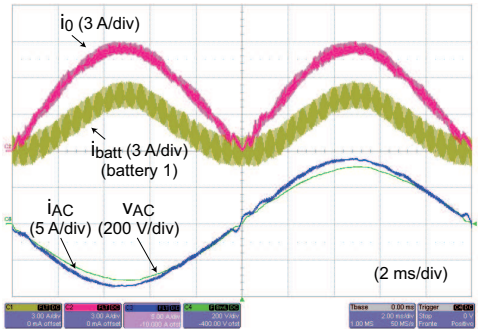

Fig. 17. Battery current with 100 Hz component. The constant PWM ripple is due to the DC/DC stage.

V. Conclusions

An integral battery charger has been proposed, modeled and experimentally tested for an electric scooter with Li-Ion batteries and anisotropic IPM motor. A multi-level PFC boost rectifier has been obtained by means of the IPM motor drive with very few additional hardware. The control of the battery charger is integrated into the control

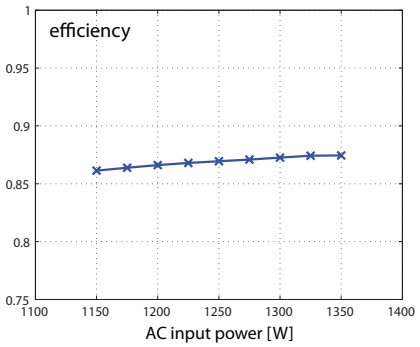

Fig. 18. Measured efficiency of the battery charger.

code of the scooter, that is performed by a fixed-point DSP controller. The analysis and the experimental results show that the IPM motor is a feasible coupling inductor for the proposed integration, that the rotor anisotropy gives no side effects and that the AC current is absorbed at unitary power factor with very limited distortion and no need for passive filtering. Induction motor and SMPM motor have been also analyzed by means of a general model and are expected to give a lower performance respect to the IPM motor. The battery current has a significant 100 Hz component, whose consequences are still under discussion in the literature.

APPENDIX: SCOOTER PROTOTYPE RATINGS

TABLE I
SCOOTER PROTOTYPE RATINGS.

Scooter		
Total weight	incl. 2 passengers	320 kg
Max Speed		90 km/h
Driving range	@ 50 km/h	130 km
Traction Power (peak)		10 kW
Batteries (2 packs)		
Voltage	nominal	260 V
Current	maximum	2 $\times$ 30 A
Weight		2 $\times$ 24 kg
Capacity		2 $\times$ 10 Ah
IPM motor drive		
Rated, max speed		2500,10000 rpm
Back-EMF	10000 rpm, phase	145 Vpk
L_d, L_q	unsat, nominal	6 mH, 40 mH
L_d, L_q	@ 20 kHz	6 mH, 10 mH
$L_0(+L_l/3)$	@ 20 kHz	1.4 mH
PWM frequency	$1/T_s$	20 kHz
dc-link voltage	traction	400 V
dc-link voltage	charge	330 V

REFERENCES

[1] J. Carlos Gomez and Medhat M. Morcos. Impact of ev battery chargers on the power quality of distribution systems. *IEEE TRANSACTIONS ON POWER DELIVERY*, 18(3):975 – 981, 2003.

[2] O. Garcia, J.A. Cobos, R. Prieto, P. Alou, and J. Uceda. Single phase power factor correction: a survey. *Power Electronics, IEEE Transactions on*, 18(3):749–755, May 2003.

[3] David Thimmesch. An scr inverter with an integral battery charger for electric vehicles. *Industry Applications, IEEE Transactions on*, IA-21(4):1023–1029, July 1985.

[4] W.E. Rippel and A.G. Cocconi. Integrated motor drive and recharge system. *US Patent*, (US005099186A), March 1992.

[5] Seung-Ki Sul and Sang-Joon Lee. An integral battery charger for four-wheel drive electric vehicle. *Industry Applications, IEEE Transactions on*, 31(5):1096–1099, Sep/Oct 1995.

[6] L. Solero. Nonconventional on-board charger for electric vehicle propulsion batteries. *IEEE TRANSACTIONS ON VEHICULAR TECHNOLOGY*, 50(1):144 – 149, 2001.

[7] R. Redl and L. Balogh. Power-factor correction in bridge and voltage-doubler rectifier circuits with inductors and capacitors. *Applied Power Electronics Conference and Exposition, 1995. APEC '95. Conference Proceedings 1995., Tenth Annual*, (0):466–472 vol.1, Mar 1995.

[8] D.J. Perreault and J.G. Kassakian. Distributed interleaving of paralleled power converters. *Circuits and Systems I: Fundamental Theory and Applications, IEEE Transactions on*, 44(8):728–734, Aug 1997.

[9] J. Salmon, A. Knight, J. Ewanchuk, and N. Noor. Multi-level single phase boost rectifiers using coupled inductors. *Power Electronics Specialists Conference, 2008. PESC 2008. IEEE*, pages 3156–3163, June 2008.

[10] E. Laboure, A. Cuniere, T.A. Meynard, F. Forest, and E. Sarraute. A theoretical approach to intercell transformers, application to interleaved converters. *Power Electronics, IEEE Transactions on*, 23(1):464–474, Jan. 2008.

[11] A. Garg, D.J. Perreault, and G.C. Verghese. Feedback control of paralleled symmetric systems, with applications to nonlinear dynamics of paralleled power converters. *Circuits and Systems, 1999. ISCAS '99. Proceedings of the 1999 IEEE International Symposium on*, 5:192–197 vol.5, 1999.

[12] H.-B. Shin, J.-G. Park, S.-K. Chung, H.-W. Lee, and T.A. Lipo. Generalised steady-state analysis of multiphase interleaved boost converter with coupled inductors. *Electric Power Applications, IEE Proceedings* -, 152(3):584–594, May 2005.

[13] Pit-Leong Wong, Peng Xu, P. Yang, and F.C. Lee. Performance improvements of interleaving vrms with coupling inductors. *Power Electronics, IEEE Transactions on*, 16(4):499–507, Jul 2001.

[14] Gaurav Nanda and Narayan C. Kar. A survey and comparison of characteristics of motor drives used in electric vehicles. *Electrical and Computer Engineering, 2006. CCECE '06. Canadian Conference on*, pages 811–814, May 2006.

[15] A.M. EL-Refaie and T.M. Jahns. Optimal flux weakening in surface pm machines using fractional-slot concentrated windings. *Industry Applications, IEEE Transactions on*, 41(3):790–800, May-June 2005.

[16] A. Affanni, A. Bellini, G. Franceschini, P. Guglielmi, and C. Tassoni. Battery choice and management for new-generation electric vehicles. *Industrial Electronics, IEEE Transactions on*, 52(5):1343–1349, Oct. 2005.

[17] D.M. Van de Sype, Koen De Gusseme, A.P.M. Van den Bossche, and J.A. Melkebeek. Duty-ratio feedforward for digitally controlled boost pfc converters. *Industrial Electronics, IEEE Transactions on*, 52(1):108–115, Feb. 2005.

[18] Hung-Chi Chen and Chih-Kai Huang. Phase feedforward control for single-phase boost-type smr. *Applied Power Electronics Conference and Exposition, 2008. APEC 2008. Twenty-Third Annual IEEE*, pages 1313–1318, Feb. 2008.

[19] F. Lacressonniere, B. Cassoret, and J.-F. Brudny. Influence of a charging current with a sinusoidal perturbation on the performance of a lead-acid battery. *Electric Power Applications, IEE Proceedings* -, 152(5):1365–1370, Sept. 2005.

[20] J. Li, E. Murphy, J. Winnick, and P.A. Kohl. The effects of pulse charging on cycling characteristics of commercial lithium-ion batteries. *Journal of Power Sources*, 102:302–309, 2001.

Gianmario Pellegrino (M06) received the M.Sc. and Ph.D. degrees in electrical engineering from the Politecnico di Torino, Turin, Italy, in 1998 and 2002, respectively. Since 2002 he is with the Department of Electrical Engineering, Politecnico di Torino, first as Research Associate and as Assistant Professor from 2007. He has been teaching power electronics and electric drives. He is involved in research projects for the public sector and for private groups, he has more than 30 technical papers and one international patent. His areas of interest are the electric drives, namely, in the motor design and digital control. He works in the fields of electric traction and of the design of direct-drive generators for wind energy production. He has been a Guest Researcher at Aalborg University, Denmark, in 2002.

Eric Armando was born in Cuneo, Italy, in 1974. He received the M.Sc. and Ph.D. degrees in electrical engineering from the Politecnico di Torino, Turin, Italy, in 2002 and 2008, respectively. He is now with Politecnico di Torino as a Research Assistant. He has been in charge of national research projects, funded by the Italian Research Ministry board, in the field of ac drives. His fields of interest are power electronics and high-performance AC motor drives.

Paolo Guglielmi (M07) was born in Imperia, Italy, in 1970. He received the M.Sc. degree in electronic engineering and the Ph.D. degree in electrical engineering from the Politecnico di Torino, Turin, Italy, in 1996 and 2001, respectively. In 1997, he joined the Department of Electrical Engineering, Politecnico di Torino, where he became a Researcher in 2002. He has authored several papers published in technical journals and conference proceedings. His fields of interest include power electronics, high-performance servodrives, and computer-aided design of electrical machines. Dr. Guglielmi is a Registered Professional Engineer in Italy.